



Analyzing the role of in situ coal fire in greenhouse gases emission in a coalfield using remote sensing data and their dispersion and source apportionment study

Shanti Swarup Biswal · Amit Kumar Gorai

Received: 21 October 2021 / Accepted: 21 April 2022 / Published online: 10 May 2022
© The Author(s), under exclusive licence to Springer Nature Switzerland AG 2022

Abstract In situ coal fires significantly pollute the environment in many countries of the world. Monitoring these pollutants is challenging due to extensive area coverage and spatial variations. Thus, the present study demonstrates the method of deriving the spatial and temporal profiles of columnar density of three major greenhouse gases (carbon monoxide (CO), sulfur dioxide (SO₂), and nitrogen dioxide (NO₂)) in an in situ coal fire region (Jharia coalfield (JCF), India) using high-resolution satellite data (TROPOMI) of the European Space Agency (ESA). The study also demonstrates a new methodology for estimating greenhouse gas emissions from in situ coal burning. JCF is one of the significant polluted mining regions with multiple in situ coal fire pockets. The columnar density of the gaseous pollutants in the mining region was compared with the same in the rural, urban, and forest regions to identify the major emission inventories. The study results indicated that coal fire is the major source of CO emission in the region, as the CO was high in the fire regions compared to that of the non-fire regions. But, the major source of NO₂ is the traffic, as the NO₂ was high in the city area as compared to other regions. The spatial profile of SO₂ does not reveal the specific emission sources. The study results indicated that TROPOMI

onboard satellite sensors could be effectively used for deriving the spatial profiles of greenhouse gaseous in coal fire regions, which further assist in identifying the emission inventories. Furthermore, the satellite-based Earth observations offer information to understand and manage the greenhouse gas emissions over a large area.

Keywords TROPOMI · Greenhouse gases emission · Air quality · Coal fires

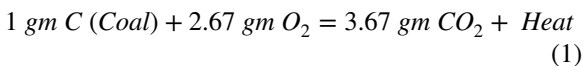
Introduction

In situ coal fire causes all types of pollution, including air, water, and land (Gielisch & Kropp, 2018). In situ coal fire emits many harmful gases (oxides and dioxides of nitrogen, carbon, and sulfur), which causes multiple health problems like lung and skin diseases (Gielisch & Kropp, 2018). Furthermore, coal fire is one of the major contributors to anthropogenic greenhouse gas emissions (Crow et al., 2019; Gielisch & Kropp, 2018; Howarth, 2014; Karavalakis et al., 2016; Thompson et al., 2011; Venkatesh et al., 2011). Coal fires lead to global climate change (Munawar, 2018) due to heat-trapping by greenhouse gases in the tropospheric region (Astrup et al., 2009; Herndon, 2018; Kweku et al., 2018; Lashof & Ahuja, 1990). The uncontrolled burning of coal seams is a natural hazard worldwide (Wessling et al., 2008). Many researchers have revealed that the burning of fossil fuels is

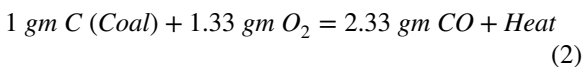
S. Swarup Biswal · A. Kumar Gorai (✉)
Department of Mining Engineering, National Institute
of Technology Rourkela, Odisha 769008, India
e-mail: amit_gorai@yahoo.co.uk

one of the significant threats to the environment and economy of a country (Braadbaart et al., 2012; Ding et al., 2013; Gurney et al., 2009; Heede, 2014; Jaeglé et al., 2005; Landry & Matthews, 2016). The primary reason for in situ coal fires is the self-combustion of coal due to illegal mining activities and abandoned coal mines. Coal burning at the subsurface level takes place with a variable oxygen supply. If the in situ coal is exposed to oxygen, spontaneous combustion of coal occurs, leading to many greenhouse gas emissions (Ozdeniz et al., 2014). The top ten greenhouse gas emitters are China, the USA, European Union, India, Russia, Japan, Brazil, Indonesia, Iran, and South Korea (Mengpin & Johanne, 2020). Thus, the gas emission characteristics are also different from the complete combustion in which the reaction takes place with a fixed oxygen supply. It is very difficult for researchers to estimate the amount of greenhouse gas emissions from in situ coal burning due to an invariable oxygen supply. The chances of complete combustion of in situ coal are less until the coal is exposed to the atmosphere or oxygen. In case of insufficient oxygen supply to coal, incomplete combustion of coal takes place. During the incomplete combustion of carbon and other elements are oxidized to form oxides of carbon, sulfur, etc. The combustion reactions that take place during in situ coal burning are as follows:

Combustion of coal in the presence of sufficient air



Combustion of coal in the presence of insufficient air



Combustion of sulfur



Coal burning emits harmful gases and emits heavy metals into the environment (UCS, 2008). The monitoring of greenhouse gas emissions is a challenging task. There are three ways (eddy covariance, measuring the temporal change of gas stocks, and measuring the concentration of atmospheric gases) to estimate the fluxes of greenhouse gases (Bréon & Ciais, 2010). Despite the vast in situ monitoring network, finer-scale estimation of global gas fluxes in the atmosphere is challenging. Also, in situ monitoring is not

possible over areas such as large water bodies and dense forests due to the region's inaccessibility. These limitations can be overcome by adopting the spaceborne remote sensing technique to monitor greenhouse gas (Chevallier et al., 2007; Palmer, 2008). The remote sensing-based approach offers uniform spatial (Liu et al., 2016; Miyazaki et al., 2017) and temporal (Lamsal et al., 2011; Richter et al., 2005) coverage in monitoring of these gases. Over the past few years, space-based observatory data have been effectively used to monitor and assess emission inventories in industrial regions by measuring various gaseous pollutants (Borrell et al., 2003; Hoff & Christopher, 2009; Martin, 2008; Palmer, 2008). The satellite instrument measures the columnar density of the gases based on the radiation absorption at a typical wavelength.

In the last few decades, many satellite sensors to monitor different gases. The European Space Agency (ESA) launched the satellite ERS-2 with a Global Ozone Monitoring Experiment (GOME) to measure O₃ and NO₂ (Burrows et al., 1997). Thereafter, ESA launched the ENVISAT satellite with the Scanning Imaging Absorption Spectrometer for Atmospheric Cartography (SCIAMACHY) sensor to measure a wide range of pollution species (Bovensmann et al., 1999), GOME-2 (Callies et al., 2000), and Infrared Atmospheric Sounding Interferometer (IASI) (Clerbaux et al., 2009) to measure CO, NH₃, and CH₄ gases. National Aeronautics and Space Administration (NASA), United States of America (USA), launched an Earth Observing System (EOS) satellite - TERRA with three sensors viz. Moderate Resolution Imaging Spectroradiometer (MODIS) (Barnes et al., 1998), Multiangle Imaging Spectroradiometer (MISR) (Diner et al., 1998), and Measurements of Pollution in the Troposphere (MOPITT) (Drummond et al., 1995) to measure the aerosol and its optical properties and CO. Thereafter, AQUA was launched by NASA with another sensor to monitor the earth's atmosphere (Lambriksen et al., 2004). Furthermore, NASA launched a satellite with two Aura sensors (Ozone Monitoring Instrument (OMI) and Tropospheric Emission Spectrometer (TES)) to understand the changing chemistry of the earth's atmosphere (Schoeberl et al., 2006), measuring the trace gases like O₃, NO₂, SO₂, HCHO, Bromine monoxide (BrO), chlorine dioxide (OCIO) (Levelt et al., 2006), and mapping of global 3-D distribution of tropospheric ozone (Beer et al., 2001). Japan Aerospace

Exploration Agency (JAXA) launched the Greenhouse gases Observing Satellite (GOSAT) to study the transport mechanism of CO₂ and CH₄ (Hamazaki et al., 2005; Kuze et al., 2006). ESA launched Sentinel 5-Precursor (S-5P) satellite (Veeffkind et al., 2012) with TROPOspheric Monitoring Instrument (TROPOMI) for monitoring air quality, climate, and the ozone layer. The S-5P sensor can measure key atmospheric constituents, including CO, SO₂, NO₂, CH₂O, and CH₄. Due to satellite data's uniform spatial and temporal resolution, the present study demonstrates the application of remote sensing-based approaches to estimate the source strength of greenhouse gases in a coal fire region. The study used TROPOMI (TROPOspheric Monitoring Instrument) onboard satellite sensor data of Sentinel-5P for estimating the spatial and temporal profiles of three greenhouse gases (CO, SO₂, and NO₂) in Jharia coalfield (JCF).

According to the Greenpeace India report, Jharia is the most polluted city in India and is a critical area of

high pollution due to coal fires. Therefore, the monitoring and assessment of greenhouse gases and their source strength identification are required for controlling the emissions from coal fires. Additionally, the columnar density of three gases (CO, SO₂, and NO₂) in the coal fire region of JCF was compared with the same in the nearby rural, urban, and forest regions for understanding the source strength of various pollutants.

Materials and method

Study area

JCF (Fig. 1) is one of India's major coalfields and primary coking coal suppliers. It is situated in the state of Jharkhand with geographical coverage of 258 km² and extends from 23°38' N to 23°49' N latitude and 86°8' E to 86°30' E longitude. JCF is situated in two districts (Dhanbad and Bokaro) of Jharkhand, and

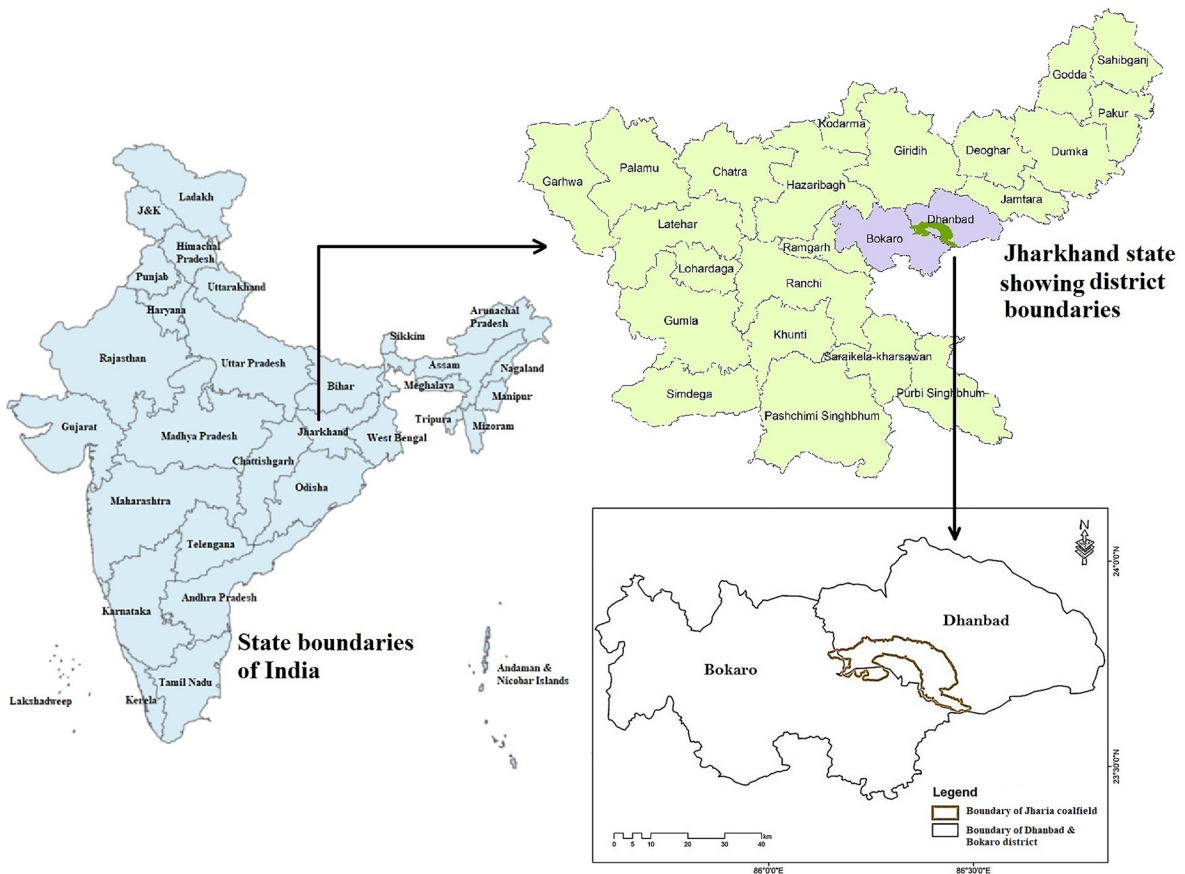


Fig. 1 Location of the study area

thus, the entire region of both districts is selected for a comparative study of pollutant levels according to different land use types.

Data used

The study used TROPOMI satellite sensor data of Sentinel-5P. TROPOMI sensor measures ultraviolet earthshine radiances at a higher spectrum. The first Copernicus mission satellite launched in October 2017, exclusively used to monitor atmospheric gases. A wide range of gases such as nitrogen dioxide (NO_2), ozone (O_3), formaldehyde (HCHO), sulfur dioxide (SO_2), carbon monoxide (CO), and methane (CH_4) can be monitored using a TROPOMI sensor. The data are provided at different time intervals depending on the level of processing like near real time (NRT), offline, and reprocessing. The present study used TROPOMI offline processed data of CO, SO_2 , and NO_2 . Vidot et al. proposed a Shortwave Infrared Carbon Monoxide Retrieval (SICOR) algorithm to estimate the CO from the S-5P sensor (Vidot et al., 2012). The retrieval of NO_2 was proposed by (van Geffen et al., 2019), which is based on the DOMINO (Dutch OMI NO_2) and QA4ECV (Quality Assurance for Essential Climate Variables) processing systems. Theys et al. (2017) have developed the retrieval of SO_2 from the TROPOMI sensor. The study also used the National Centers for Environmental Prediction (NCEP)/National Center for Atmospheric Research (NCAR) Reanalysis 1 dataset

of wind speed and direction for dispersion analysis. The region's daily wind speed and direction data are available online at NOAA Physical Science Laboratory (PSL) of the USA. The CO, NO_2 , and SO_2 concentrations in microgram per cubic meter along with metrological parameters like temperature ($^{\circ}\text{C}$), relative humidity (%), solar radiation (W/m^2), and barometric pressure (mmHg) were used for the multiple linear regression analyses. These data were obtained from the Central Pollution Control Board website from the environmental pollution data section (Source: <https://cpcb.nic.in/automatic-monitoring-data/>).

Methods

The flowchart of the working methodology is shown in Fig. 2. The working methodology involves three major stages viz. satellite data processing for retrieval of monthly means of columnar density for selected gaseous pollutants for the specified duration, visualization of retrieval data for the study region, and analyzing the data to understand the emission characteristics in different region climatic conditions.

Sentinel-5P data available in the Google Earth Engine (GEE) are used for estimating the CO, SO_2 , and NO_2 over the Jharia coalfield. The spatial profiles of the monthly mean of three pollutants were derived for the study region for the year 2019. The spatial maps of monthly means of columnar density were generated using the code editor in GEE and finally processed in ArcGIS for visualization

Fig. 2 Flowchart of the working methodology

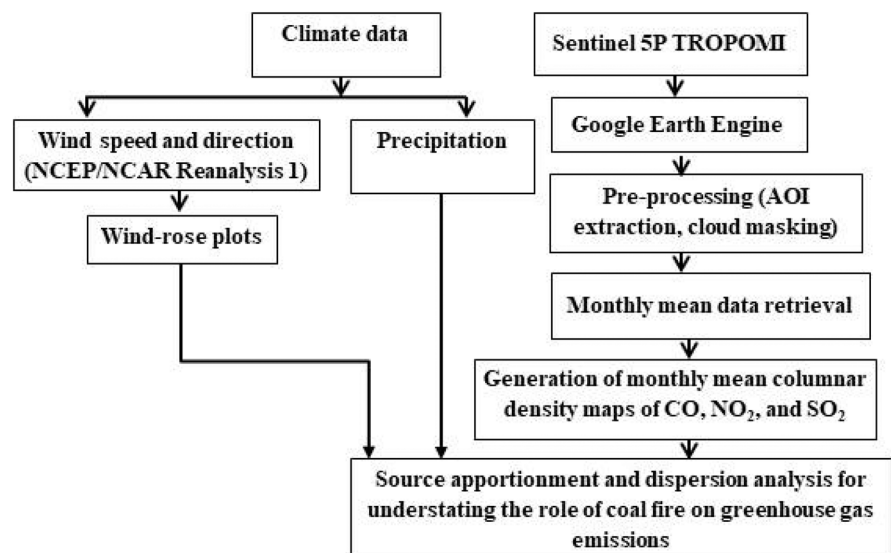


Table 1 Location details of different land use types in the study area

Station no.	Name	Latitude	Longitude	Description
S1	Tisra fires	23.721	86.443	Fire zone
S2	Angarapathara fires	23.805	86.318	Fire zone
S3	Katras fires	23.786	86.304	Fire zone
S4	Lodna fires	23.722	86.420	Fire zone
S5	Kusunda Godhar fires	23.774	86.395	Fire zone
S6	Bokaro Steel Plant	23.665	86.121	Urban area
S7	Parasnath Hill, Tundi	23.965	86.376	Forest/hilly region
S8	Lugu Pahar	23.777	85.709	Forest/hilly region
S9	Village Area	23.603	85.934	Rural area

and analysis. Preprocessing of the satellite data includes AOI extraction and cloud masking.

The monthly means were extracted for each month of 2019. Nine specific locations (Table 1) from four land use types (coal fire mining region, urban region, rural, and forest area) were chosen for comparative analysis of the monthly means of columnar density with land use types (Fig. 3). Out of nine stations, five (S1, S2, S3, S4, and S5), located in JCF, represent the coal fires; one (S6), situated in Bokaro steel city,

represent industrial or urban region; two (S7, S8), situated in the two major hills with an elevation of 893 m and 1365 m, represent the forest area; and one (S9), located in a village, represents the rural area.

The windrose plots for the same periods were also generated using NCEP-NCAR reanalysis data for the nearest location (86.250° N, 23.809° E) of the Jharia coalfield for understanding the dispersion behaviors of these gases. The wind speed and direction data are derived from the v-wind and u-wind components.

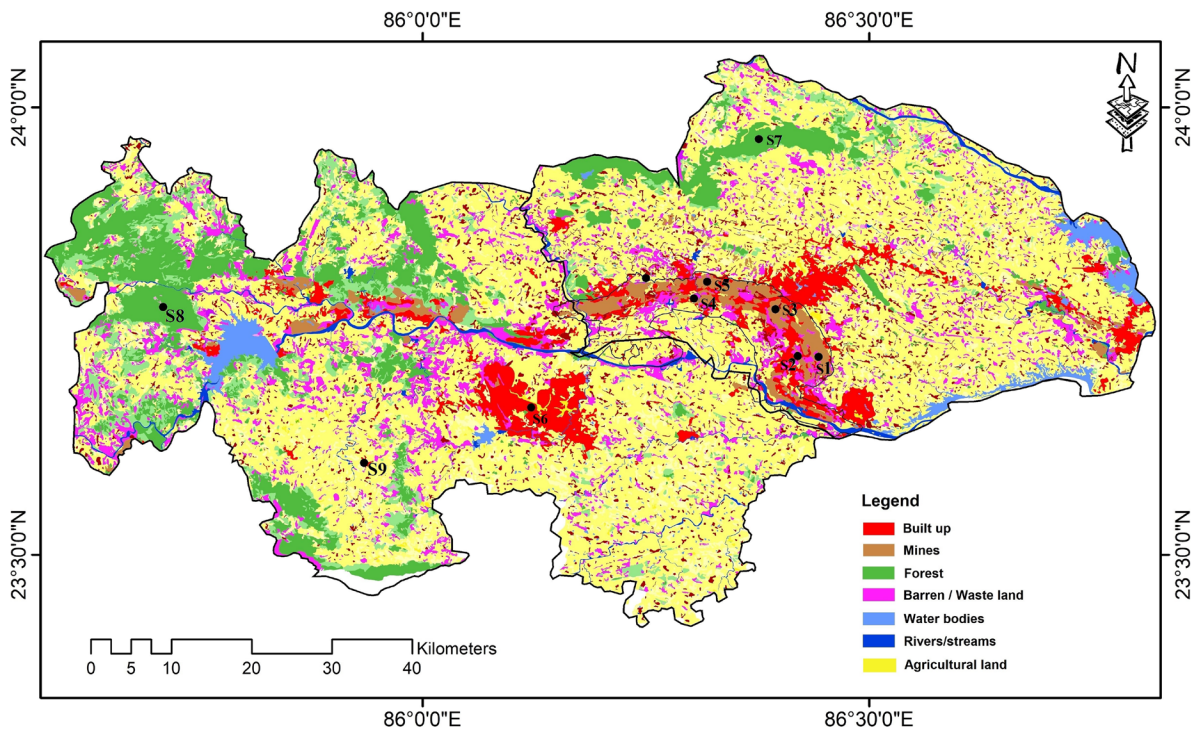


Fig. 3 Land use/landcover map of the study area

The monthly windrose diagrams are generated for the year 2019. Similarly, the monthly average precipitation data for the year 2019 was used for analyzing its influence on the emission of gases.

The multiple linear regression analyses were performed to examine the dependency of TROPOMI-based columnar density and other metrological parameters (temperature, relative humidity, wind speed, solar radiation, and barometric pressure) with the ground-level pollution concentration. In this model, the concentration of gases obtained from CPCB was considered a dependent variable and columnar density of gases along with other meteorological parameters were regarded as independent or predictor variables.

Results and discussion

The spatial maps for CO, NO₂, and SO₂ were derived using GEE and processed using ArcGIS. The spatial maps from January 2019 to December 2019 for each month were derived for CO, NO₂, and SO₂. The monthly mean precipitation level along with the windspeed for 2019 was plotted (shown in Fig. 4) to study the effects of rainfall on greenhouse gas emissions. The windrose plots of each month of the year 2019 were also prepared and shown with the respective month's spatial map.

Spatio-temporal variation of columnar density of CO

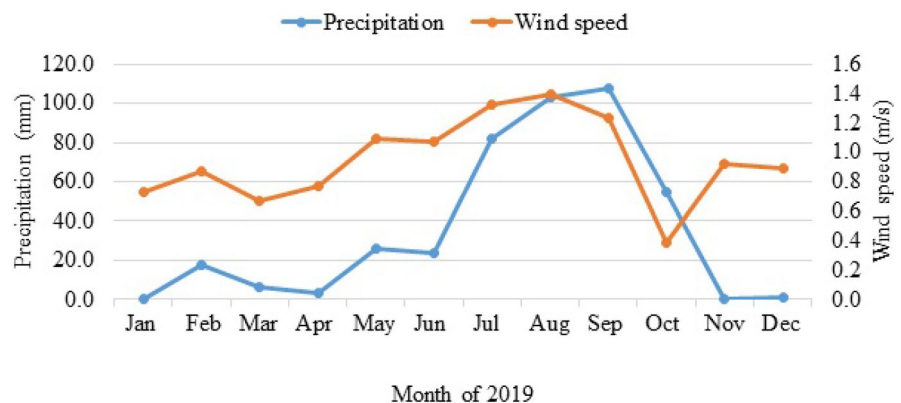
The spatial distributions of the monthly mean of CO (mol/m²) are shown in Fig. 5a–l for the year 2019. It can be inferred from the monthly mean map that a higher value of CO was observed in the southeastern

regions, i.e., in most of the months except during monsoon months (July, August, and September). The monthly precipitations (shown in Fig. 4) indicate high precipitation levels in these 3 months. The results indicate that columnar density during monsoon months (July (0.035–0.041), August (0.033–0.037), September (0.033–0.040), and October (0.038–0.048)) are lower in comparison to the other months ((January (0.039–0.055), February (0.035–0.052), March (0.039–0.055), April (0.044–0.057), May (0.040–0.056), June (0.043–0.052), November (0.039–0.062), December (0.039–0.060)).

The highest value was observed during the winter months (November and December), as the gas dispersion was low due to calm atmospheric conditions. It was also observed that CO mainly concentrated over the Jharia coalfield and Bokaro Steel Plant, which indicates that coal fire and the steel plant are the major sources of CO emissions.

The monthly means of CO were also extracted for nine locations of different land use types, as shown in Fig. 6. Out of these nine points, five locations represent the mining area (S1, S2, S3, S4, and S5), one represents the urban or industrial area (S6), two represent the hilly/forest area (S7 and S8), and one represents the village area (S9). In most of the locations, CO was highest in November and December. The higher concentration in these 2 months is low dispersion, as the wind speed was relatively lower during these months (shown in Fig 4). The monthly mean of CO were found to be higher in fire areas (S1, S2, S3, S4, and S5) and steel plant (S6) than the stations located in forest/hilly areas (S7 and S8) and village area (S9). The results indicate that coal fire and the Bokaro steel plant are the two major sources of CO emission in the study region.

Fig. 4 Monthly average precipitation and rainfall chart



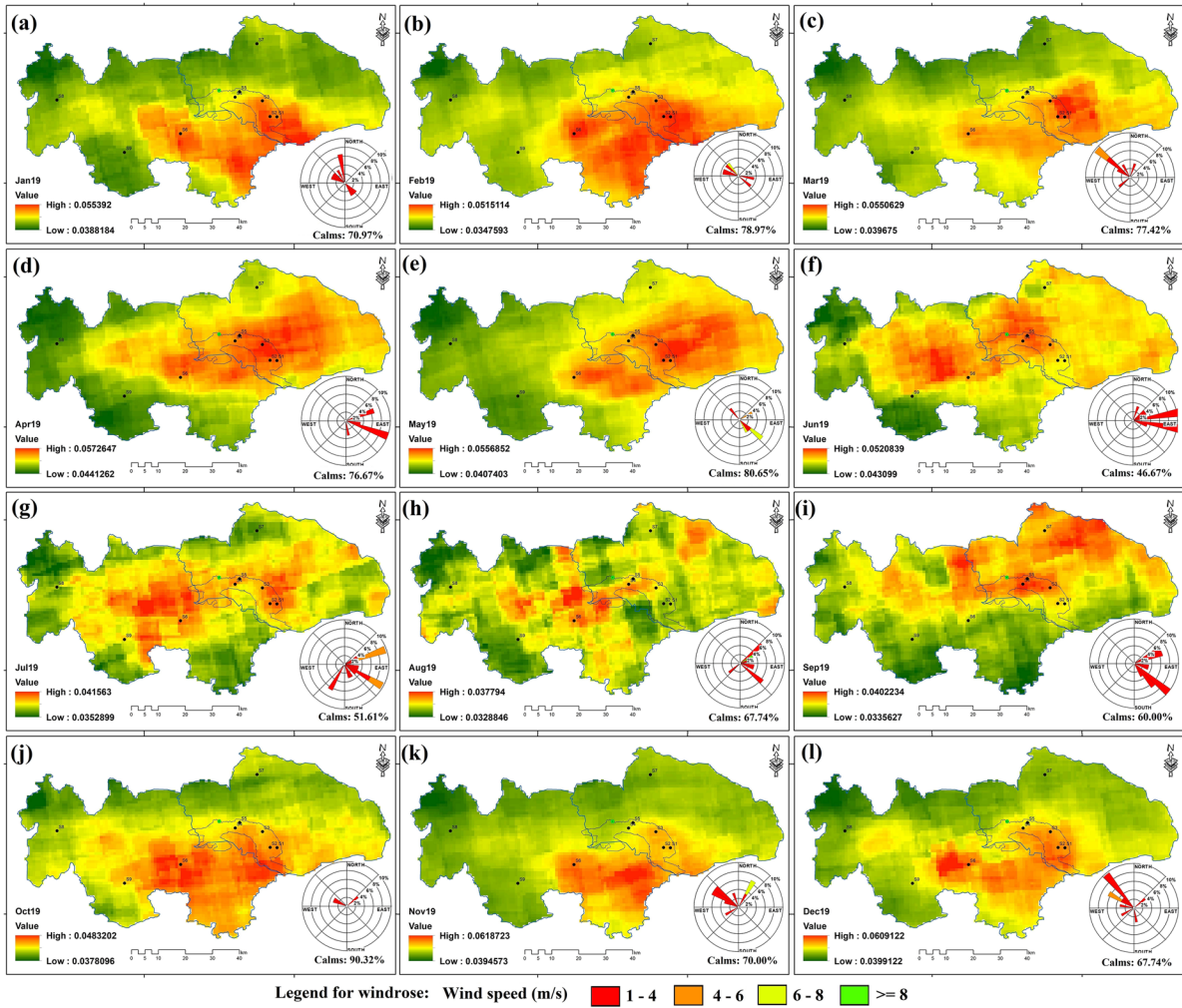
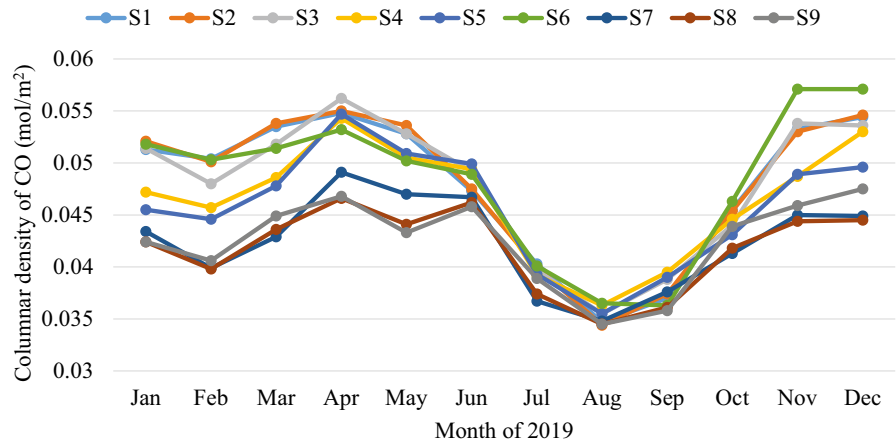


Fig. 5 CO column density map (a) January (b) February (c) March (d) April (e) May (f) June (g) July (h) August (i) September (j) October (k) November (l) December

Fig. 6 Monthly means of columnar density of CO in different locations



Spatio-temporal variation of columnar density of NO₂

The monthly means of the columnar density map of NO₂ (mol/m²) is derived in the Google Earth engine for the year 2019, as represented in Fig. 7a–l. In most cases, the derived monthly means indicate a higher value in the mining and urban regions (Bokaro Steel city) except in September. The maximum monthly mean for NO₂ was found to be 0.00015591, 0.000158976, 0.000160008, 0.000146958, 0.000122054, 0.000110367, 0.0000798774, 0.0000737129, 0.0000996758, 0.000110612, 0.000160898, and 0.000146346 respectively in January, February, March, April, May, June, July, August, September, October, November, and December. In this case, the maximum values of the monthly mean are found to be lowest during the monsoon months (July, August, and September).

It can also be inferred from the spatial maps that the highest NO₂ was mainly concentrated over the Bokaro steel plant and Jharia coalfield across the study area in most of the months.

The columnar density of NO₂ was extracted for the nine selected locations, as shown in Fig. 8. It was observed that NO₂ was highest in the Bokaro steel plant region (S6) in each month for the study period in comparison to the mining regions (S1, S2, S3, S4, and S5). The monthly means of columnar density of NO₂ were found to be lowest in village

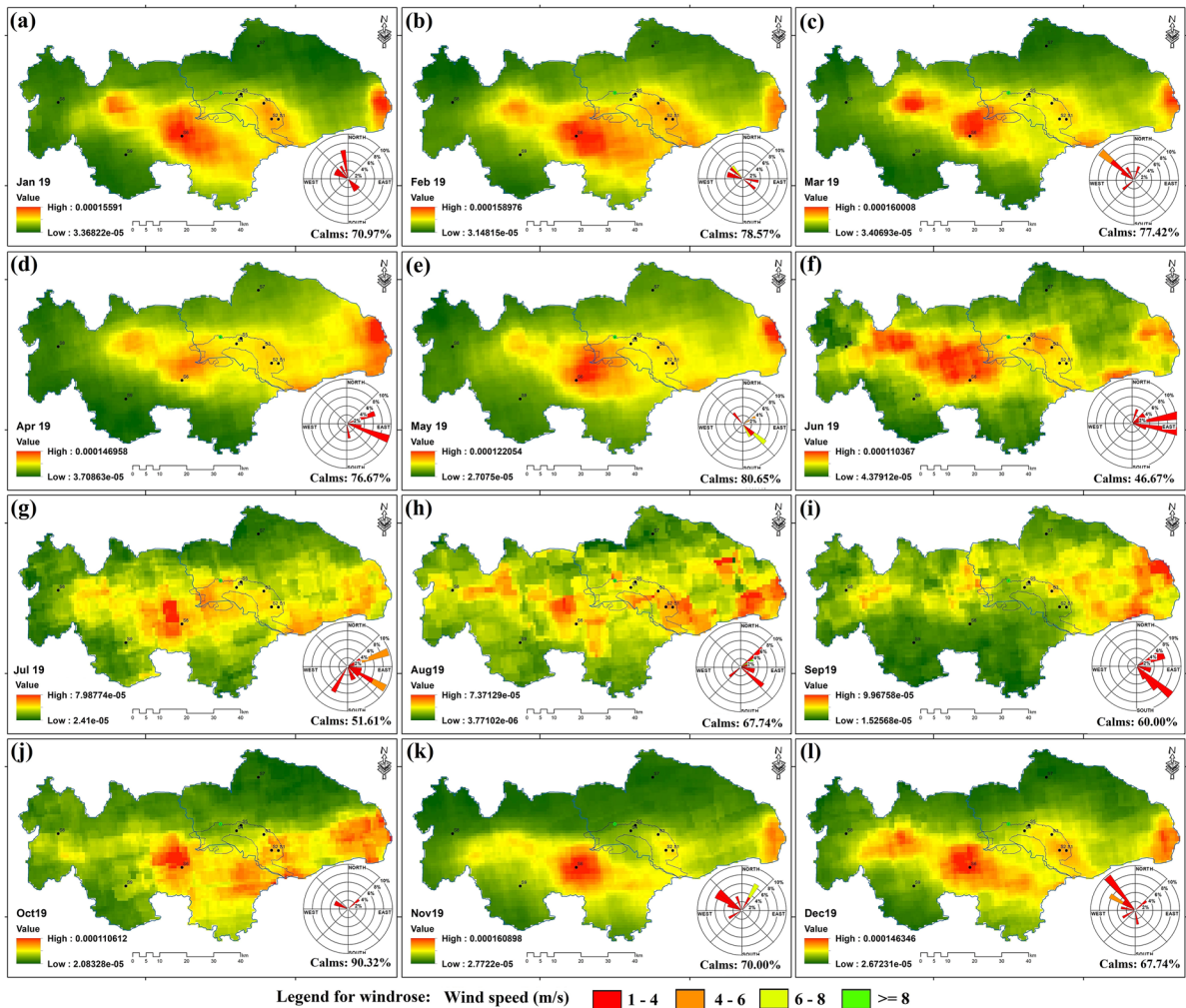
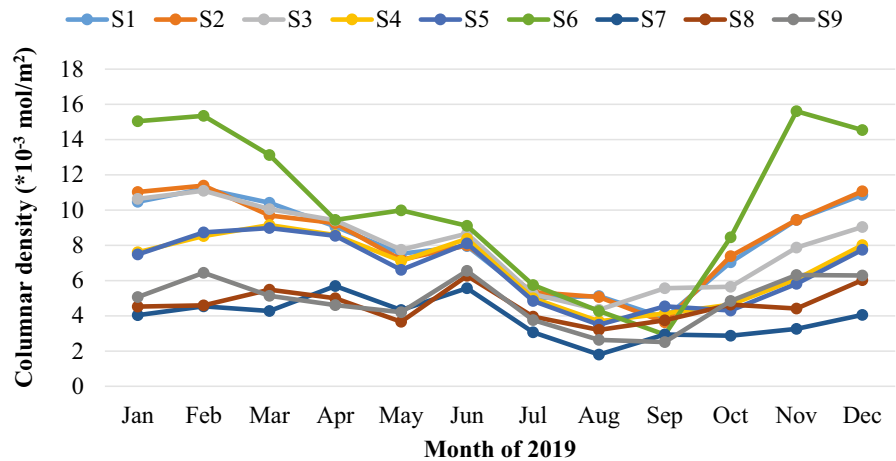


Fig. 7 NO₂ columnar density map (a) January (b) February (c) March (d) April (e) May (f) June (g) July (h) August (i) September (j) October (k) November (l) December

Fig. 8 Monthly means of columnar density of NO₂ in different locations



and forest areas (S7, S8, and S9). Therefore, it can be presumed that most of the emissions of NO₂ are from vehicular emissions in the urban area (Bokaro steel plant) and coal fires.

Spatio-temporal variation of columnar density of SO₂

The spatial distributions of the monthly mean columnar density of SO₂ (mol/m²) are shown in Fig. 9a–l for 2019. These values were extracted for nine locations (S1-S9) of different land use types to analyze the distributions and sources (Fig. 10). The SO₂ was observed to be low during monsoon months (July to September). In these months, the columnar densities of SO₂ in rural and forest regions (S7, S8, and S9) were found to be below the detection level. The negative values indicate a clean area or having low SO₂ levels (Theys et al., 2017). In most cases, the columnar density of SO₂ was found to be highest over the mining and urban areas (S1, S2, S3, S4, S5, and S6), but the values did not show any specific trend. The spatial maps were not showing any hotspot of higher SO₂ by which an inference on emissions source can be identified.

Source apportionment and dispersion analyses of gaseous CO, NO₂, and SO₂

Though the maximum CO and NO₂ concentrations were observed near the emission sources on most occasions, the locations of recorded maximum CO and NO₂ concentrations varied with time. The prime

reason behind this is the influence of horizontal dispersion of gaseous pollutants due to higher wind speed. The wind rose plots for each month are shown along with the spatial maps of CO, NO₂, and SO₂ (Figs. 5a–l, 7a–l, and 9a–l). The windrose diagrams were generated using WRPLOT software version 8.0.2. The windrose diagrams indicate that the region has significant wind speed variations and directions with the season. The wind speed in the regions has either calm (0–1 m/s) or in the range of 1–4 m/s, and thus, the horizontal dispersion of pollutants is low. In March 2019, the wind speed exceeded 4 m/s 10% of the time, and the prevailing wind direction is N-W and S-E. Thus, the gaseous pollutants from mining regions are transported towards the S-E direction. This leads to a higher columnar density of CO and NO₂ in the S-E region. In June 2019, more than 10 % of wind reached a speed greater than 4 m/s, and the prevailing wind direction was from E-N-E to W-S-W and from E-S-E to W-N-W. Therefore, most of the gases are concentrated towards the west of the emission sources.

For analyzing the strength of TROPOMI-based estimations of CO, NO₂, and SO₂, a multiple regression analysis was done by considering respective columnar density as a dependent variable and meteorological data (wind speed, temperature, relative humidity, and barometric pressure) along with the respective pollutant concentrations (CO/NO₂/SO₂) as dependent variables. The daily concentrations of CO, NO₂, and SO₂ and meteorological data from 1 January 2019 to 31 December 2019 were obtained

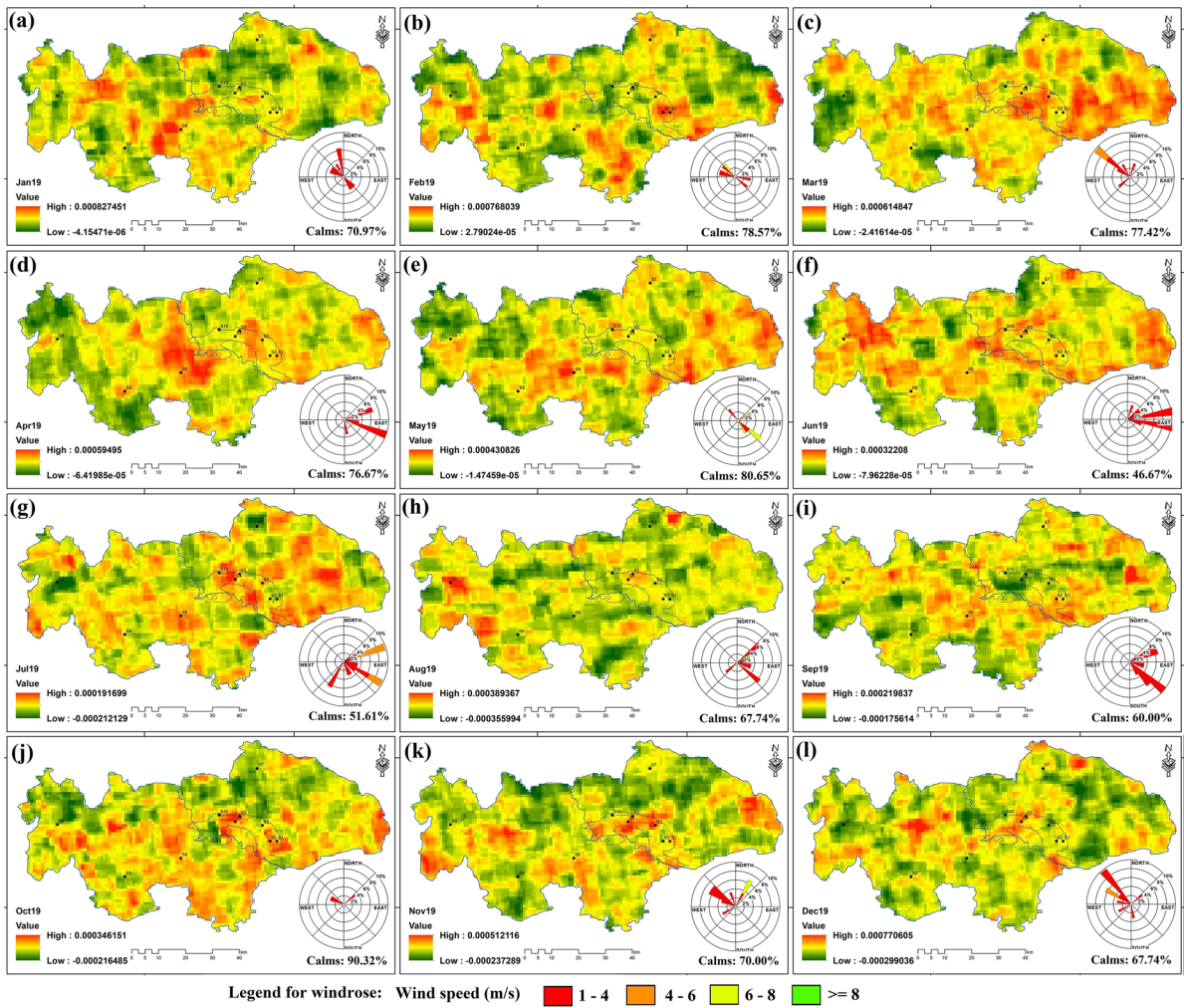
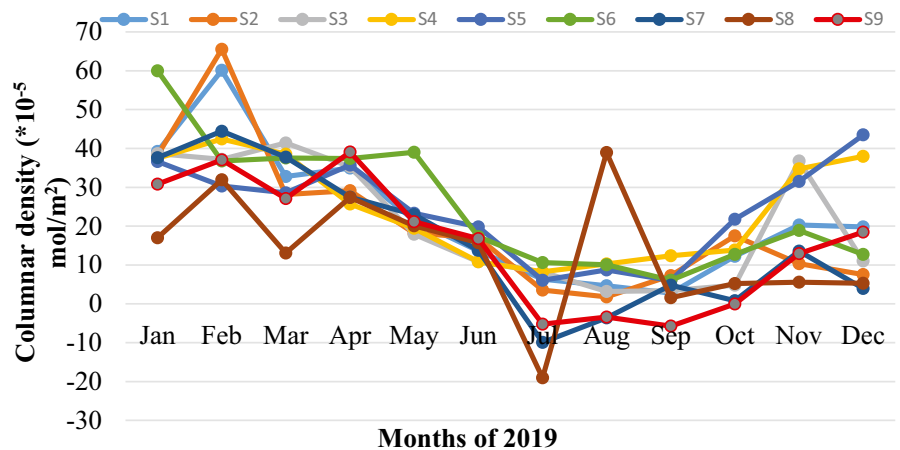


Fig. 9 SO₂ columnar density map (a) January (b) February (c) March (d) April (e) May (f) June (g) July (h) August (i) September (j) October (k) November (l) December

Fig. 10 Monthly means of columnar density of SO₂ (10⁻⁵) in different locations



for Jorapokhar, Jharkhand (latitude: 23.707909, longitude: 86.414670) from the CPCB website (<https://cpcb.nic.in/automatic-monitoring-data/>). The results of the multiple regression analyses are presented in Table 2. The R^2 values for CO, NO₂, and SO₂ were 0.316, 0.295, and 0.598, respectively. Though the R^2 values are less in each case, the regression models are statistically significant in each case. All the models are statistically significant at a 5% significance level, as the F values are less than 0.05 in each case. The results further indicate that wind speed has a negative influence on each pollutant, as the coefficients are -0.264 , -0.040 , and -0.018 , respectively, for CO, NO₂, and SO₂. For CO, all the predictor variables have a negative influence except barometric pressure. Interestingly, temperature and relative humidity showed a positive influence, and the rest of the parameters showed negative influences on NO₂ concentrations. For SO₂, all the predictor variables showed negative influence except columnar density on observed concentration. It should be noted that all the dependent variables are statistically significant at a 5% significance level for the prediction of CO concentrations except solar radiation and columnar density. It was also observed no dependent variables are statistically significant at a 5% significance level for the prediction of NO₂ concentrations except barometric pressure. For SO₂, all the dependent variables are statistically significant at a 5% significance level except wind speed. Thus, it can be inferred from the results that TROPOMI-based columnar depth can be used for tracking and estimations of SO₂ only. The remote sensing-based approach for estimation of greenhouse gases emission for a small region is explained in the subsequent section.

Estimation of greenhouse gases emission from in situ coal fire

In this study, a remote sensing-based approach is used to estimate greenhouse gas emissions from in situ coal fires. The demarcated area is represented in the coal fire map of JCF for 2019 (Fig. 11), which was obtained from Biswal and Gorai (2021). JCF has a large number of working mines, and few of them are affected by coal fires. The red areas showed the subsurface fires in 2019. In this study, a small area was considered to quantify the gas emission

Table 2 Multiple regression analyses results

Item	No. of data	R^2	Sig. F	Statistical parameter	Wind speed (m/s)	Temperature (°C)	Relative humidity (%)	Solar radiation (W/m ²)	Barometric pressure (mmHg)	TROPOMI (mol/m ²)
CO	56	0.316	0.004	Coefficient	-0.264	-0.493	-0.412	-0.225	0.407	-0.065
				SE	0.018	0.016	0.003	0.001	0.043	4.766
				P value	0.034	0.008	0.041	0.128	0.019	0.670
NO ₂	204	0.295	0.000	Coefficient	-0.040	0.215	0.061	-0.049	-0.714	-0.028
				SE	0.039	0.029	0.004	0.001	0.070	1264.114
				P value	0.513	0.181	0.430	0.563	0.000	0.708
SO ₂	188	0.598	0.000	Coefficient	-0.018	-0.227	-0.242	-0.180	-0.359	0.163
				SE	0.992	0.704	0.096	0.025	1.631	4156.901
				P value	0.704	0.064	0.000	0.010	0.003	0.001

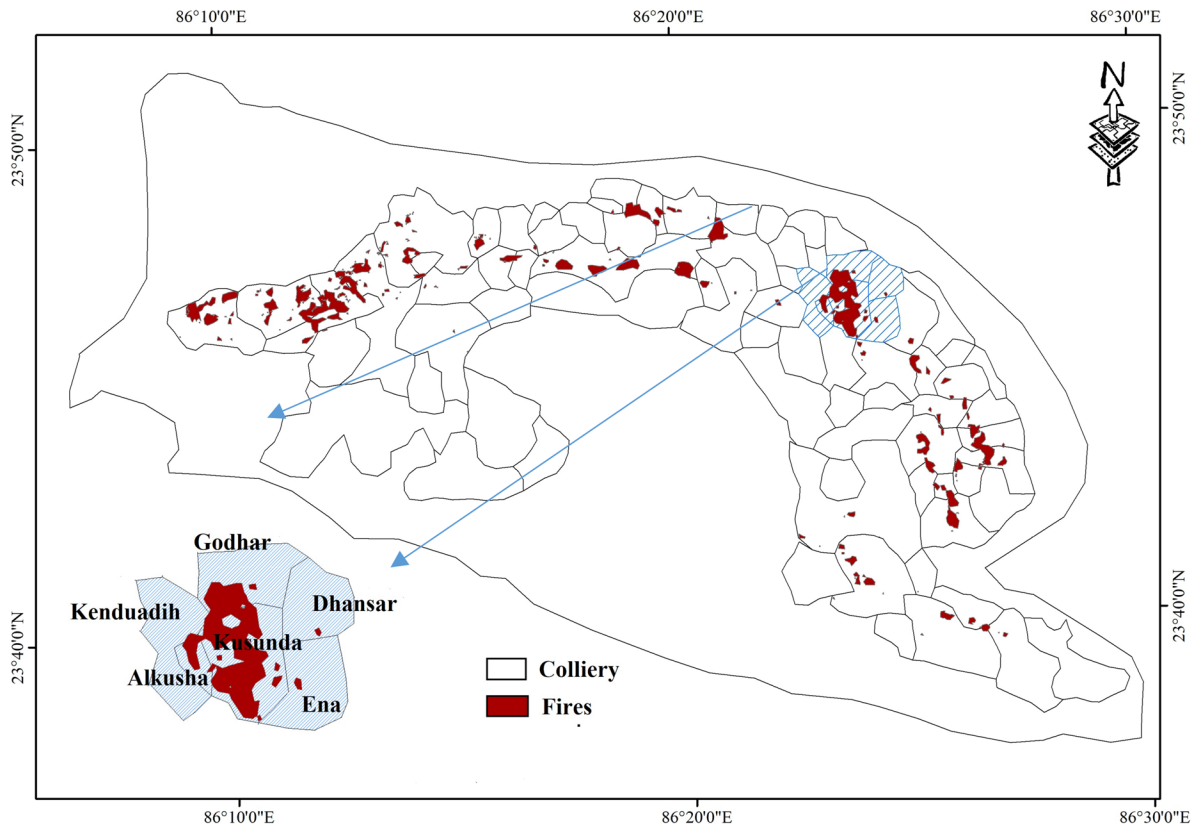


Fig. 11 Colliery map showing the coal fire pockets in 2019

from in situ coal burning due to the availability of coal seam details.

The selected area comprises six collieries (Kenduadih, Godhar, Kusunda, Alkusha, Ena, and Dhansar), as indicated in Fig. 11. The reserves in this area are confined to the Barakar coal measures (Lower Permian), which contain twenty-four coal seams (Mineral Exploration Corporation Limited, 2013). The in situ coal extends to a depth of 610 m and has a total reserve of 11,728 million tonnes (Mehta et al., 1957). The total surface area coverage of six collieries (study area) was estimated to be 10.2 km². The quality of coal in this reserve was classified as high-grade metallurgical and sub-bituminous. The specific gravity of coal was assumed to be 1.346 kg per cubic meter. Past studies indicated that coal fires were existed in seams XI and XII of JCF from 2008 to 2016 (Hamilton et al., 2009; Mohalik et al., 2016). This suggests that seams XI and XII were under fire and were not completely extinguished from 2008 to 2016. The study estimated the

gas emission from 2009 to 2019 based on the coal fire maps of 2009 and 2019 (Fig. 12) (for a detailed description of the coal fire maps, refer to the manuscript of Biswal & Gorai, 2020, 2021). The average thickness values of coal seams XI and XII are 7.31 m and 3.63 m, respectively (Mohalik et al., 2016).

The area coverages of coal fire for 2009 and 2019 were estimated to be 1.91 km² and 0.89 km² respectively. Thus, it is assumed that entire coal is burned for the area of 0.276 km² (= 1.91–0.89) in 10 years (2009 to 2019). Therefore, the volume of coal burned can be determined as follows:

$$\begin{aligned}
 &\text{Volume of coal burned during 2009 to 2019} \\
 &= \text{Surface area of coal burned} \\
 &\quad \times (\text{thickness of XI seam} + \text{thickness of XII seam}) \\
 &= 276000\text{m}^2 \times (7.31\text{m} + 3.63\text{m}) = 3019440\text{m}^3
 \end{aligned}$$

The weight of coal burned can be determined by multiplying the volume of coal burned to the specific

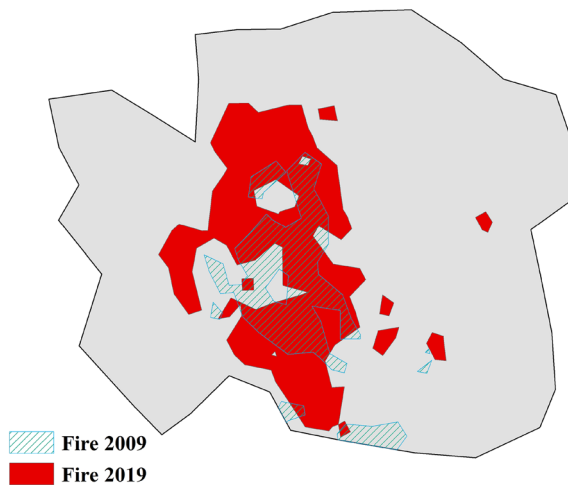


Fig. 12 Coal fire map in 2009 and 2019 in AOI

gravity of coal (1.346 kg/m^3), which was estimated as 4,064,166.24 kg.

Equations (2) and (3) indicate that 1 g of coal burning under complete combustion emits 2.33 g and 2 g of CO and SO₂, respectively. Therefore, 4,064,166.24 kg of coal burns emits approximately 9.4695 Mt of CO and 8.128 Mt of SO₂, respectively. In the same way, CO₂ emission can also be estimated.

Conclusions

The study demonstrates the use of Sentinel-5P observations in deriving the spatial profiles of three gaseous pollutants (CO, NO₂, and SO₂) over JCF. The study selects nine locations of four land use types (mining region, steel plant city, forest/hilly area, and village area) for identifying the major emission sources. The study results show that CO was high in the fire regions as compared to the non-fire areas. However, the columnar density of NO₂ was high in the Bokaro steel city as compared to other regions. Coal-mining regions exhibit a higher value for NO₂ but less than the urban area. The reason is that the urban area in this location mainly comprises industries whose NO₂ emissions might be more than the emissions from coal fires. This indicates that coal-mining activities are the major source of CO, whereas the vehicular and steel industry is the major source of NO₂. The spatial profile of SO₂ does not reveal the specific emission source,

as there was no specific trend observed with different land use types. The point data at nine locations indicates that SO₂ was low in the rural area as compared to other land use types. Thus, the TROPOMI data can efficiently identify the major emission sources for air quality management in a region. The greenhouse gas emission results indicated that approximately 9.4695 Mt of CO and 8.128 Mt of SO₂ has been emitted in 10 years (2009 to 2019) only from six collieries based on the assumptions that entire coal is burned with complete combustion.

Acknowledgements The authors are acknowledged to NIT Rourkela for providing the computing facility and Google Earth Engine group for providing the Google Earth Engine cloud platform and freely available datasets (Sentinel 5P).

Author contribution Shanti Swarup Biswal: conceptualization, methodology, software, investigation, validation, writing-original draft, visualization. Amit Kumar Gorai: conceptualization, methodology, software, investigation, writing-review and editing, visualization, supervision

Availability of data and materials The datasets analyzed during the current study are available on the Google Earth Engine platform. All data generated during this study are included in this published article.

Declarations

Ethics approval and consent to participate Not applicable.

Consent to publish Not applicable.

Competing interests The authors declare no competing interests.

References

Astrup, T., Møller, J., & Fruergaard, T. (2009). Incineration and co-combustion of waste: Accounting of greenhouse gases and global warming contributions. *Waste Management and Research*, 27(8), 789–799. <https://doi.org/10.1177/0734242X09343774>

Barnes, W. L., Pagano, T. S., & Salomonson, V. V. (1998). Pre-launch characteristics of the moderate resolution imaging spectroradiometer (MODIS) on EOS-AMI. *IEEE Transactions on Geoscience and Remote Sensing*, 36(4), 1088–1100. <https://doi.org/10.1109/36.700993>

Beer, R., Glavich, T. A., & Rider, D. M. (2001). Tropospheric emission spectrometer for the Earth Observing System’s Aura satellite. *Applied Optics*, 40(15), 2356. <https://doi.org/10.1364/ao.40.002356>

- Biswal, S. S., & Gorai, A. K. (2020). Change detection analysis in coverage area of coal fire from 2009 to 2019 in Jharia Coalfield using remote sensing data. *International Journal of Remote Sensing*, 41(24), 9545–9564. <https://doi.org/10.1080/01431161.2020.1800128>
- Biswal, S. S., & Gorai, A. K. (2021). Studying the coal fire dynamics in Jharia coalfield, India using time-series analysis of satellite data. *Remote Sensing Applications: Society and Environment*, 23, 100591. <https://doi.org/10.1016/j.rsase.2021.100591>
- Borrell, P., Burrows, J. P., Richter, A., Platt, U., & Wagner, T. (2003). New directions: New developments in satellite capabilities for probing the chemistry of the troposphere. *Atmospheric Environment*, 37(18), 2567–2570. [https://doi.org/10.1016/S1352-2310\(03\)00150-X](https://doi.org/10.1016/S1352-2310(03)00150-X)
- Bovensmann, H., Burrows, J. P., Buchwitz, M., Frerick, J., Noël, S., Rozanov, V. V., et al. (1999). SCIAMACHY: Mission objectives and measurement modes. *Journal of the Atmospheric Sciences*, 56(2), 127–150. [https://doi.org/10.1175/1520-0469\(1999\)056%3c0127:SMOAMM%3e2.0.CO;2](https://doi.org/10.1175/1520-0469(1999)056%3c0127:SMOAMM%3e2.0.CO;2)
- Braadbaart, F., Poole, I., Huisman, H. D. J., & van Os, B. (2012). Fuel, Fire and Heat: An experimental approach to highlight the potential of studying ash and char remains from archaeological contexts. *Journal of Archaeological Science*, 39(4), 836–847. <https://doi.org/10.1016/j.jas.2011.10.009>
- Bréon, F. M., & Ciais, P. (2010). Spaceborne remote sensing of greenhouse gas concentrations. *Comptes Rendus - Geoscience*, 342(4–5), 412–424. <https://doi.org/10.1016/j.crte.2009.09.012>
- Burrows, J. P., Buchwitz, M., Rozanov, V., Weber, M., Richter, A., Ladstätter-Weißmayer, A., & Eisinger, M. (1997). The Global Ozone Monitoring Experiment (GOME): Mission, instrument concept, and first scientific results. *European Space Agency, (Special Publication) ESA SP*, 56(414 PART 2), 585–590.
- Callies, J., Corpaccioli, E., Eisinger, M., Hahne, A., & Lefebvre, A. (2000). GOME-2-Metop's second-generation sensor for operational ozone monitoring. *ESA bulletin*, 102, 28–36.
- Chevallier, F., Bréon, F. M., & Rayner, P. J. (2007). Contribution of the Orbiting Carbon Observatory to the estimation of CO₂ sources and sinks: Theoretical study in a variational data assimilation framework. *Journal of Geophysical Research Atmospheres*, 112(9). <https://doi.org/10.1029/2006JD007375>
- Clerbaux, C., Boynard, A., Clarisse, L., George, M., Hadji-Lazarou, J., Herbin, H., et al. (2009). Monitoring of atmospheric composition using the thermal infrared IASI/MetOp sounder. *Atmospheric Chemistry and Physics*, 9(16), 6041–6054. <https://doi.org/10.5194/acp-9-6041-2009>
- Crow, D. J. G., Balcombe, P., Brandon, N., & Hawkes, A. D. (2019). Assessing the impact of future greenhouse gas emissions from natural gas production. *Science of the Total Environment*, 668, 1242–1258. <https://doi.org/10.1016/j.scitotenv.2019.03.048>
- Diner, D. J., Beckert, J. C., Reilly, T. H., Bruegge, C. J., Conel, J. E., Kahn, R. A., et al. (1998). Multi-angle imaging spectroradiometer (MISR) instrument description and experiment overview. *IEEE Transactions on Geoscience and Remote Sensing*, 36(4), 1072–1087. <https://doi.org/10.1109/36.700992>
- Ding, A. J., Fu, C. B., Yang, X. Q., Sun, J. N., Petäjä, T., Kerminen, V. M., et al. (2013). Intense atmospheric pollution modifies weather: A case of mixed biomass burning with fossil fuel combustion pollution in eastern China. *Atmospheric Chemistry and Physics*, 13(20), 10545–10554. <https://doi.org/10.5194/acp-13-10545-2013>
- Drummond, J. R., Bailak, G. V., & Mand, G. (1995). The Measurements of Pollution in the Troposphere (MOPITT) Instrument. In *Applications of Photonic Technology* (pp. 197–200). https://doi.org/10.1007/978-1-4757-9247-8_38
- Gielisch, H., & Kropp, C. (2018). Coal fires a major source of greenhouse gases- a forgotten problem. *Environmental Risk Assessment and Remediation*, 02(01). <https://doi.org/10.4066/2529-8046.100030>
- Gurney, K. R., Mendoza, D. L., Zhou, Y., Fischer, M. L., Miller, C. C., Geethakumar, S., & Du Can, S. D. L. R. (2009). High-resolution fossil fuel combustion CO₂ emission fluxes for the United States. *Environmental Science and Technology*, 43(14), 5535–5541. <https://doi.org/10.1021/es900806c>
- Hamazaki, T., Kaneko, Y., Kuze, A., & Kondo, K. (2005). Fourier transform spectrometer for Greenhouse Gases Observing Satellite (GOSAT). In *Enabling Sensor and Platform Technologies for Spaceborne Remote Sensing* (Vol. 5659, p. 73). <https://doi.org/10.1117/12.581198>
- Hamilton, M., McLachlan, R. S., & Burneo, J. G. (2009). Can I go out for a smoke? A nursing challenge in the epilepsy monitoring unit. *Seizure*, 18(4), 285–287. <https://doi.org/10.1016/j.seizure.2008.11.002>
- Heede, R. (2014). Tracing anthropogenic carbon dioxide and methane emissions to fossil fuel and cement producers, 1854–2010. *Climatic Change*, 122(1–2), 229–241. <https://doi.org/10.1007/s10584-013-0986-y>
- Herndon, J. M. (2018). Air pollution, not greenhouse gases: The principal cause of global warming. *Journal of Geography, Environment and Earth Science International*, 17(2), 1–8. <https://doi.org/10.9734/jgeesi/2018/44290>
- Hoff, R. M., & Christopher, S. A. (2009). Remote sensing of particulate pollution from space: Have we reached the promised land? *Journal of the Air and Waste Management Association*, 59(6), 645–675. <https://doi.org/10.3155/1047-3289.59.6.645>
- Howarth, R. W. (2014). A bridge to nowhere: Methane emissions and the greenhouse gas footprint of natural gas. *Energy Science and Engineering*, 2(2), 47–60. <https://doi.org/10.1002/ese3.35>
- Jaeglé, L., Steinberger, L., Martin, R. V., & Chance, K. (2005). Global partitioning of NO_x sources using satellite observations: Relative roles of fossil fuel combustion, biomass burning and soil emissions. *Faraday Discussions*, 130, 407–423. <https://doi.org/10.1039/b502128f>
- Karavalakis, G., Hajbabaie, M., Jiang, Y., Yang, J., Johnson, K. C., Cocker, D. R., & Durbin, T. D. (2016). Regulated, greenhouse gas, and particulate emissions from lean-burn and stoichiometric natural gas heavy-duty vehicles on different fuel compositions. *Fuel*, 175, 146–156. <https://doi.org/10.1016/j.fuel.2016.02.034>
- Kuze, A., Kondo, K., Hamazaki, T., Oguma, H., Morino, I., Yokota, T., & Inoue, G. (2006). Greenhouse gases monitoring from the GOSAT satellite. *Journal of the Remote Sensing Society of Japan*, 26(1), 41–42. <https://doi.org/10.11440/rssj1981.26.41>

Kweku, D., Bismark, O., Maxwell, A., Desmond, K., Danso, K., Oti-Mensah, E., et al. (2018). Greenhouse effect: Greenhouse gases and their impact on global warming. *Journal of Scientific Research and Reports*, 17(6), 1–9. <https://doi.org/10.9734/jsrr/2017/39630>

Lambriksen, B., Fetzer, E., Fishbein, E. Lee, S. Y., Pagano, T. (2004). AIRS - The atmospheric infrared sounder International Geoscience and Remote Sensing Symposium (IGARSS) 2204–2207 <https://doi.org/10.1364/opn.2.10.00025>

Lamsal, L. N., Martin, R. V., Padmanabhan, A., Van Donkelaar, A., Zhang, Q., Sioris, C. E., et al. (2011). Application of satellite observations for timely updates to global anthropogenic NOx emission inventories. *Geophysical Research Letters*, 38(5). <https://doi.org/10.1029/2010GL046476>

Landry, J. S., & Matthews, H. D. (2016). Non-deforestation fire vs. fossil fuel combustion: The source of CO₂ emissions affects the global carbon cycle and climate responses. *Biogeosciences*, 13(7), 2137–2149. <https://doi.org/10.5194/bg-13-2137-2016>

Lashof, D. A., & Ahuja, D. R. (1990). Relative contributions of greenhouse gas emissions to global warming. *Nature*, 344(6266), 529–531. <https://doi.org/10.1038/344529a0>

Levelt, P. F., Van Den Oord, G. H. J., Dobber, M. R., Mälkki, A., Visser, H., de Vries, J., Stammes, P., Lundell, J. O. V., & Saari, H. (2006). The Ozone Monitoring Instrument. *IEEE Transactions on Geoscience and Remote Sensing*, 44(5), 1093–1101. <https://doi.org/10.1109/TGRS.2006.872333>

Liu, R., Men, C., Liu, Y., Yu, W., Xu, F., & Shen, Z. (2016). Spatial distribution and pollution evaluation of heavy metals in Yangtze estuary sediment. *Marine Pollution Bulletin*, 110(1), 564–571. <https://doi.org/10.1016/j.marpolbul.2016.05.060>

Martin, R. V. (2008). Satellite remote sensing of surface air quality. *Atmospheric Environment*, 42(34), 7823–7843. <https://doi.org/10.1016/j.atmosenv.2008.07.018>

Mehta, D. R. S., Narayana Murthy, B. R., & Fox, C. S. (1957). *A revision of the geology and coal resources of the Jharia coalfield*. Manager of Publications.

Mengpin, G., & Johannes, F. (2020). 4 Charts Explain Greenhouse Gas Emissions by Countries and Sectors. *World Resources Institute*. <https://www.wri.org/blog/2020/02/greenhouse-gas-emissions-by-country-sector>. Accessed 8 February 2021

Mineral Exploration Corporation limited. (2013). *Geological report on coal exploration production support drilling* (Vol. 1).

Miyazaki, K., Eskes, H., Sudo, K., Folkert Boersma, K., Bowman, K., & Kanaya, Y. (2017). Decadal changes in global surface NOx emissions from multi-constituent satellite data assimilation. *Atmospheric Chemistry and Physics*, 17(2), 807–837. <https://doi.org/10.5194/acp-17-807-2017>

Mohalik, N. K., Lester, E., Lowndes, I. S., & Singh, V. K. (2016). Estimation of greenhouse gas emissions from spontaneous combustion/fire of coal in opencast mines—Indian context. *Carbon Management*, 7(5–6), 317–332. <https://doi.org/10.1080/17583004.2016.1249216>

Munawar, M. E. (2018). Human health and environmental impacts of coal combustion and post-combustion wastes. *Journal of Sustainable Mining*, 17(2), 87–96. <https://doi.org/10.1016/j.jsm.2017.12.007>

Ozdeniz, H., Sivrikaya, O., Sensogut, C. (2014). Mine planning and equipment selection Mine Planning and Equipment Selection 637–644. <https://doi.org/10.1007/978-3-319-02678-7>

Palmer, P. I. (2008). Quantifying sources and sinks of trace gases using spaceborne measurements: Current and future science. *Philosophical Transactions of the Royal Society A: Mathematical, Physical and Engineering Sciences*, 366(1885), 4509–4528. <https://doi.org/10.1098/rsta.2008.0176>

Richter, A., Burrows, J. P., Nüß, H., Granier, C., & Niemeier, U. (2005). Increase in tropospheric nitrogen dioxide over China observed from space. *Nature*, 437(7055), 129–132. <https://doi.org/10.1038/nature04092>

Schoeberl, M. R., Douglass, A. R., Hilsenrath, E., Bhartia, P. K., Beer, R., Waters, J. W., et al. (2006). Overview of the EOS aura mission. *IEEE Transactions on Geoscience and Remote Sensing*, 44(5), 1066–1072. <https://doi.org/10.1109/TGRS.2005.861950>

Theys, N., De Smedt, I., Yu, H., Danckaert, T., Van Gent, J., Hörmann, C., et al. (2017). Sulfur dioxide retrievals from TROPOMI onboard Sentinel-5 Precursor: Algorithm theoretical basis. *Atmospheric Measurement Techniques*, 10(1), 119–153. <https://doi.org/10.5194/amt-10-119-2017>

Thompson, W., Whistance, J., & Meyer, S. (2011). Effects of US biofuel policies on US and world petroleum product markets with consequences for greenhouse gas emissions. *Energy Policy*, 39(9), 5509–5518. <https://doi.org/10.1016/j.enpol.2011.05.011>

UCS. (2008). Coal and Air Pollution. *Union of Concerned Scientists*. <https://www.ucsusa.org/resources/coal-and-air-pollution>. Accessed 14 December 2020

van Geffen, J. H. G. M., Eskes, H. J., Boersma, K. F., Maasackers, J. D., & Veefkind, J. P. (2019). TROPOMI ATBD of the total and tropospheric NO₂ data products. *S5p/TROPOMI*, (1.4.0), 1–76. <https://sentinel.esa.int/documents/247904/2476257/Sentinel-5P-TROPOMI-ATBD-NO2-data-products>

Veefkind, J. P., Aben, I., McMullan, K., Förster, H., de Vries, J., Otter, G., et al. (2012). TROPOMI on the ESA Sentinel-5 Precursor: A GMES mission for global observations of the atmospheric composition for climate, air quality and ozone layer applications. *Remote Sensing of Environment*, 120, 70–83. <https://doi.org/10.1016/j.rse.2011.09.027>

Venkatesh, A., Jaramillo, P., Griffin, W. M., & Matthews, H. S. (2011). Uncertainty analysis of life cycle greenhouse gas emissions from petroleum-based fuels and impacts on low carbon fuel policies. *Environmental Science and Technology*, 45(1), 125–131. <https://doi.org/10.1021/es102498a>

Vidot, J., Landgraf, J., Hasekamp, O. P., Butz, A., Galli, A., Tol, P., & Aben, I. (2012). Carbon monoxide from short-wave infrared reflectance measurements: A new retrieval approach for clear sky and partially cloudy atmospheres. *Remote Sensing of Environment*, 120, 255–266. <https://doi.org/10.1016/j.rse.2011.09.032>

Wessling, S., Kessels, W., Schmidt, M., & Krause, U. (2008). Investigating dynamic underground coal fires by means of numerical simulation. *Geophysical Journal International*, 172(1), 439–454. <https://doi.org/10.1111/j.1365-246X.2007.03568.x>

Publisher’s Note Springer Nature remains neutral with regard to jurisdictional claims in published maps and institutional affiliations.